Tractable molecular theory of transport of Lennard-Jones fluids in nanopores

Suresh K. Bhatia, Owen Jepps, and David Nicholson

Citation: The Journal of Chemical Physics **120**, 4472 (2004); doi: 10.1063/1.1644108
View online: http://dx.doi.org/10.1063/1.1644108
View Table of Contents: http://scitation.aip.org/content/aip/journal/jcp/120/9?ver=pdfcov
Published by the AIP Publishing

Tractable molecular theory of transport of Lennard-Jones fluids in nanopores

Suresh K. Bhatia,[a] Owen Jepps, and David Nicholson
Division of Chemical Engineering, The University of Queensland, Brisbane QLD 4072, Australia

(Received 5 August 2003; accepted 3 December 2003)

We present here a tractable theory of transport of simple fluids in cylindrical nanopores, which is applicable over a wide range of densities and pore sizes. In the Henry law low-density region the theory considers the trajectories of molecules oscillating between diffuse wall collisions, while at higher densities beyond this region the contribution from viscous flow becomes significant and is included through our recent approach utilizing a local average density model. The model is validated by means of equilibrium as well nonequilibrium molecular dynamics simulations of supercritical methane transport in cylindrical silica pores over a wide range of temperature, density, and pore size. The model for the Henry law region is *exact* and found to yield an excellent match with simulations at all conditions, including the single-file region of very small pore size where it is shown to provide the density-independent collective transport coefficient. It is also shown that in the absence of dispersive interactions the model reduces to the classical Knudsen result, but in the presence of such interactions the latter model drastically overpredicts the transport coefficient. For larger micropores beyond the single-file region the transport coefficient is reduced at high density because of intermolecular interactions and hindrance to particle crossings leading to a large decrease in surface slip that is not well represented by the model. However, for mesopores the transport coefficient increases monotonically with density, over the range studied, and is very well predicted by the theory, though at very high density the contribution from surface slip is slightly overpredicted. It is also seen that the concept of activated diffusion, commonly associated with diffusion in small pores, is fundamentally invalid for smooth pores, and the apparent activation energy is not simply related to the minimum pore potential or the adsorption energy as generally assumed. [DOI: 10.1063/1.1644108]

I. INTRODUCTION

The transport of molecules in nanopores and confined spaces is a problem of long-standing importance in heterogeneous catalysis, gas-solid reactions, and adsorptive separations, with a history dating back to the early work of Knudsen.[1] In recent years intense worldwide activity in the applications of newly developed templated and molecularly imprinted materials, carbon nanotubes, as well as a host of other microporous and mesoporous materials has led to renewed interest in the subject.[2,3] Nevertheless, despite the long history, understanding is still far from satisfactory for pores of nanoscale dimension and models largely empirical even for pores of ideal shape.[4]

In his seminal work Knudsen[1] analyzed the momentum transfer processes at the pore walls assuming diffuse reflection, in the absence of any intermolecular as well as wall–molecule interactions. He thereby determined a transport coefficient for cylindrical pores, which is concentration independent and applicable to low pressures at which the mean free path is much greater than the pore diameter. Knudsen's treatment was subsequently modified in a more elaborate analysis by von Smoluchowski,[5] who considered the molecular trajectories in the pore and corrected Knudsen's result by a small factor of $3\pi/8$. Further refinement was provided by Pollard and Present[6] in a classic analysis that considered also collision processes in the pore when the mean free path is smaller than the pore diameter. These profound developments accurately apply to noninteracting systems, where they predict the surface slip arising from diffuse reflection at the pore wall. However, there are no equivalent results to date for systems with realistic interactions, although formal theories in this direction have been proposed.[7,8] Because of the limited tractability of these theories, it is still common to use empirical formulations for nanopores smaller than about 2 nm, considered to be in the ''configurational'' or ''activated'' diffusion regime[4] where the transport is strongly influenced by interactions. For larger pores it is common to use the framework of the dusty gas formulation of Mason *et al.*,[9] while ignoring interactions in the spirit of the Knudsen and related treatments,[1,5,6] to estimate fluxes and transport coefficients. In this approach the transport model superposes diffusive and viscous flows, so that for pure component flow in a cylindrical pore

$$j_z = -\left(D_0 + \frac{r_p^2 \hat{\rho} k_B T}{8\eta} \right) \frac{\hat{\rho}}{k_B T} \nabla_z \mu, \tag{1}$$

in which D_0 is a diffusion coefficient, r_p is the pore radius measured from the center of the surface LJ sites, and η is a mean viscosity. The second term in the parentheses on the

[a]Author to whom correspondence should be addressed: Fax: +61 7 3365 4263. Electronic mail: sureshb@cheque.uq.edu.au

right-hand side represents the contribution from viscous flow. The latter is based on the established Hagen–Poiseuille model, obtained by solving the Navier–Stokes equation assuming no slip at the wall and uniform pressure over the cross section. The mechanistic interpretation of the diffusion coefficient D_0 is, however, somewhat less certain, as discussed above, and varies from that of a Knudsen diffusivity for gaseous phase transport[9] to surface diffusivity when a dense adsorbate phase is involved.[4] From Eq. (1) a Fickian coefficient is obtained by application of the Darken thermodynamic factor to obtain[10]

$$D_t=\left(D_0+\frac{r_p^2\hat{\rho}k_BT}{8\eta}\right)\left(\frac{\partial \ln(f)}{\partial \ln(\hat{\rho})}\right)_T, \tag{2}$$

which assumes equilibrium over the pore cross section. Here f is a pseudo-gas-phase fugacity that would be in equilibrium with the pore fluid at the mean adsorbed number density $\hat{\rho}$.

In recent communications from this laboratory[11,12] several fundamental weaknesses in the above formulation have been identified, apart from the empirical nature of the diffusion coefficient D_0. The most significant of these is the use of a uniform mean density $\hat{\rho}$ and mean viscosity coefficient η, averaged over the pore cross section in the application of the Poiseuille flow model in Eq. (1). While this may be acceptable in large pores at high densities near saturation, at low densities (i.e., low bulk fugacities) and in narrow pores a strong density profile exists due to the effect of the adsorbent potential field and these assumptions are unsatisfactory. In addition, there is an inconsistency in the above formulation in that while the Poiseuille flow model is derived based on the assumption of a uniform pressure over the pore cross section, the application of the Darken factor in Eq. (2) assumes a uniform chemical potential (i.e., thermodynamic equilibrium) over the same cross section. Because a strong nonuniform density profile exists normal to the pore wall, particularly at low and moderate densities, this assumption violates the Gibbs–Duhem relation.

A more refined application of the Navier–Stokes equations has been proposed by Bitsanis *et al.*[13] who allow for viscosity variations over the pore cross section by evaluating the local viscosity at a coarse-grained density,

$$\overline{\rho}(\mathbf{r})=\frac{6}{\pi\sigma_f^3}\int_{|\mathbf{r}'|<\sigma_f/2}\rho(\mathbf{r}+\mathbf{r}')d\mathbf{r}', \tag{3}$$

obtained upon local averaging of the density over a sphere of radius $\sigma_f/2$, where σ_f is the molecular diameter. However, their analysis also assumes a uniform pressure over the cross section, while using the equilibrium density profiles (i.e., assuming a uniform chemical potential over the cross section), in violation of the Gibbs–Duhem relation. In addition, their approach uses a no-slip condition at the pore surface and therefore predicts a vanishing transport coefficient at low densities that is contrary to experiment.[4]

Some progress towards the incorporation of interactions, while overcoming the above modeling deficiencies, has recently been achieved in our laboratory[11,12] by approximating the location of the diffuse reflection as that of the minimum of the fluid–solid potential. Consideration of the momentum transfer processes at this location, combined with viscous flow in the pore in the presence of density gradients, provides a satisfactory, though not quantitatively exact, explanation of the concentration dependence of the transport coefficient over a wide range of densities and pore sizes. In these studies the modified equation of motion in cylindrical geometry,

$$\frac{1}{r}\frac{d}{dr}\left[r\eta(r)\frac{du_z}{dr}\right]=\rho(r)\frac{d\mu}{dz}, \tag{4}$$

obtained upon combining the Navier–Stokes and Gibbs–Duhem equations, has been solved assuming cross-sectional equilibrium, with a frictional condition at the pore wall,

$$k\rho_0u_0=-\eta\frac{du_z}{dr} \quad \text{at } r=r_0, \tag{5}$$

which considers perfectly diffuse reflection at the location, r_0, of the minimum of the fluid–solid interaction potential. Here u_0 is the streaming velocity at $r=r_0$ (i.e., the slip velocity). The left-hand side of Eq. (5) represents the rate of momentum loss due to diffuse reflection for particles crossing the potential minimum while moving towards the wall. Further, k is a friction coefficient and ρ_0 the local reference density at r_0. The wall collision frequency for particles crossing the potential minimum is assumed to depend on this density and, based on kinetic theory considerations, $k=\sqrt{mk_BT/2\pi}$. Further, it may be noted that while molecules will have zero net axial velocity immediately after diffuse reflection, Eq. (4) implicitly assumes that they equilibrate with the incident molecules and attain the streaming velocity u_0 over a vanishingly small distance. This assumption is necessary because the viscous model used in the interior region is valid only for a fluid in microscopic local equilibrium. In actual fact a nonequilibrium region must exist before the viscous model becomes applicable, but this is assumed to be small and of negligible influence. Solution of Eqs. (4) and (5) provides the axial streaming velocity profile $u_z(r)$ and the axial flux j_z following $j_z=2[\int_0^{r_0}ru_z(r)\rho(r)dr]/r_p^2$. Use of the phenomenological relation

$$j_z=\frac{D_{t0}\hat{\rho}}{k_BT}(-\nabla\mu) \tag{6}$$

then leads to the transport coefficient

$$D_{t0}(\hat{\rho})=\frac{2k_BT}{\hat{\rho}r_p^2}\left[\frac{1}{kr_0\rho_0}\left(\int_0^{r_0}r\rho(r)dr\right)^2+\int_0^{r_0}\frac{dr}{r\eta(\overline{\rho}(r))}\left(\int_0^r r'\rho(r')dr'\right)^2\right], \tag{7}$$

in which the local viscosity is obtained via the locally averaged density model (LADM) in Eq. (3). Equation (7) is consistent with the general dusty gas model form [cf. Eqs. (1) and (2)], superposing diffusive (or surface slip) and viscous contributions represented by the first and second terms in parentheses, respectively. However, the underlying kinetic theory assumes uncorrelated Maxwellian distributions of velocities in the three principal directions at the potential minimum location in estimating the friction factor, which is inac-

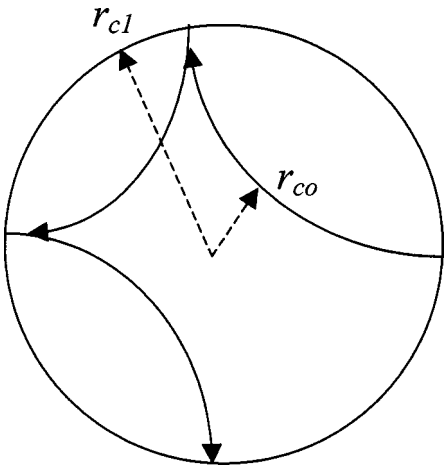

FIG. 1. Schematic of trajectories of an oscillating molecule projected onto the pore cross section.

curate at low pressures at which intermolecular collisions are infrequent. The theory also neglects penetration of the repulsive region of the solid–fluid potential as it assumes diffuse reflection at the location of the potential minimum itself.

Here we develop a new theory for the diffusive term that is exact for low pressures where intermolecular interactions are negligible and the fluid–solid interaction dominates. The model solves the Hamiltonian dynamics of the molecules oscillating between diffuse wall reflections in the potential field due to the solid and makes no assumption about the location of the point of reflection, which is obtained from the solution of the equations of motion. It is shown that a modified theory combining this diffusive part with the viscous contribution in Eq. (7) accurately predicts transport coefficients over a wide range of pore sizes and temperatures, except for high densities where, as discussed previously,[11,12] the surface slip is drastically reduced and alternate, dense phase, theories may be more appropriate. For validation of the theory equilibrium and nonequilibrium molecular dynamics (EMD and NEMD, respectively) computations have been performed and are reported here. A brief initial report of the low-density theory is also provided elsewhere.[14]

II. TRANSPORT MODEL

We first develop here a theory for the transport coefficient of a Lennard-Jones (LJ) fluid at low pressures in the conservative external potential field of a cylindrical pore. To this end we consider a particle moving in the pore under the influence of this external potential and an applied axial force f. The latter represents the applied force in NEMD simulations or, in effect, a chemical potential gradient $(-\nabla\mu)$. Such a particle when moving towards the wall is reflected at some radial position r_{c1} at which its radial velocity becomes zero and it reverses direction. Under these circumstances the particle will execute an oscillating or hopping motion, as depicted (front view) in Fig. 1, in which the particle trajectory has a point of closest approach to the center located at radial position r_{c0}. Since the external potential field due to the pore walls is conservative, the radial location of the point of reflection, r_{c1}, is the same on both ends of the trajectory (i.e., a single oscillation). At this position r_{c1}, it is assumed that diffuse reflection occurs in the tangent $(\theta\text{-}z)$ plane. This idealized diffuse reflection model for the surface is not necessarily an accurate representation of a real solid adsorbent, as demonstrated in recent studies of atomically detailed surfaces.[15,16] Reflection from atomically smooth surfaces (such as graphitic materials) is quite close to being purely specular, while even from surfaces that are quite rough on the atomic scale, reflection can be more than 50% specular. Recent studies[17] with single-wall carbon nanotubes have shown a relatively smooth energy landscape that would favor nearly specular reflection and high transport coefficients. However, the theory to be developed can be readily extended to accommodate any other reflection condition, and for the purposes of illustrating the development the idealized diffuse reflection condition suffices. Significantly, this is also the condition embedded in the widely used Knudsen theory[1,5] of the transport coefficient in hard sphere systems. In this connection it should be noted that the above studies with atomically detailed surfaces[15–17] have considered idealized defect-free systems, which is perhaps somewhat unrealistic. Real carbons, for example, are quite defective with a high degree of disorder, as confirmed in laboratory studies and interpretation of x-ray diffractograms of heat-treated carbons.[18,19] In addition, reverse Monte Carlo–determined carbon structures based on interpretations of x-ray diffraction structure factors, as well as transmission electron microscopy studies, reveal the presence of a high degree of disorder in carbons and even suggest the presence of a large number of rings having fewer than six members in graphene planes.[20] In such materials the fraction of specularly reflected particles is likely to be significantly less than that from defect-free surfaces, and the choice of appropriate boundary conditions is therefore somewhat ambiguous. In this scenario and in the absence of definitive boundary conditions, the diffuse reflection condition suffices for the purpose of the present development.

Under conditions of steady flow the transport coefficient may be related to the mean hopping time $\langle\tau\rangle$ of the trajectory by means of the phenomenological equation

$$\langle u_z\rangle = \frac{D_{t0}}{k_B T} f = \frac{f}{m}\langle\tau\rangle, \tag{8}$$

in which $\langle u_z\rangle$ is the mean streaming velocity in the pore and $f\langle\tau\rangle$ represents the mean axial momentum gain in a single oscillation. Equation (8) represents a somewhat different approach than an early attempt[21] at computing the flux in confined spaces under a concentration gradient by averaging the product of path length and axial velocity obtained from numerically computed trajectories. Equation (8) suggests that the flux is instead determined by the mean oscillation or ''hopping'' time of a trajectory. Further, we shall treat the trajectories analytically rather than numerically, leading to dramatic savings in computational time. Equation (8) leads to the transport coefficient

$$D_{t0} = \frac{k_B T}{m}\langle\tau\rangle, \tag{9}$$

in which the quantity $m/\langle\tau\rangle$ may be viewed as an Einstein friction coefficient. As defined above, the transport coeffi-

cient is based on a chemical potential gradient driving force and must be multiplied by the Darken thermodynamic factor [cf. Eq. (2)] to obtain the Fickian transport diffusivity. To determine the oscillation time for an arbitrary trajectory we solve the equations of motion

$$\frac{dp_r}{dt} = -\frac{\partial H}{\partial r}, \tag{10}$$

$$\frac{dr}{dt} = \frac{\partial H}{\partial p_r}, \tag{11}$$

$$\frac{dp_z}{dt} = -\frac{\partial H}{\partial z}, \tag{12}$$

for a particle with Hamiltonian

$$H = V(r) + \frac{p_r^2}{2m} + \frac{p_\theta^2}{2mr^2} + \frac{p_z^2}{2m} - zf \tag{13}$$

in a conservative radial potential field $V(r)$. Here we choose $z=0$ at the point of diffuse reflection where the particle reverses direction. Since there is no tangential force, angular momentum is conserved—i.e., $p_\theta = \text{const}$ during the motion. Equations (12) and (13) readily yield

$$p_z = ft + p_{z0}, \tag{14}$$

where p_{z0} is the random axial momentum after diffuse reflection at r_{c1}. Since $\langle p_{z0}\rangle = 0$ for diffuse reflection, we obtain $\langle u_z\rangle = f\langle\tau\rangle/m$, where the averaging is performed with respect to the distributions of p_r, p_θ, and p_{z0}. Further, Eq. (14) is readily integrated to yield

$$z = \frac{p_{z0}}{m}t + \frac{f}{2m}t^2, \tag{15}$$

which combines with Eq. (14) to provide

$$\frac{p_z^2}{2m} - fz = \frac{p_{z0}^2}{2m}, \tag{16}$$

thereby ensuring that the Hamiltonian in Eq. (13) is conservative.

At low pressures for which intermolecular interactions in the adsorbed phase are negligible $V(r) = \phi_{fs}(r)$, where $\phi_{fs}(r)$ is the one-dimensional position-dependent external potential due to the solid–fluid interaction in the pore. Substitution of Eq. (13) into Eqs. (10) and (11) provides

$$\frac{dp_r}{dr} = -\frac{m}{p_r}\left(\frac{\partial \phi_{fs}}{\partial r} - \frac{p_\theta^2}{mr^3}\right), \tag{17}$$

whose integration yields the radial momentum profile for particles moving towards the pore wall:

$$p_r(r', r, p_r, p_\theta) = \left\{ 2m[\phi_{fs}(r) - \phi_{fs}(r')] + p_r^2(r) + \frac{p_\theta^2}{r^2}\left(1 - \frac{r^2}{r'^2}\right)\right\}^{1/2}. \tag{18}$$

Here $p_r(r', r, p_r, p_\theta)$ is the radial momentum at position r' for a particle having radial momentum p_r at position r. Equations (11) and (13) now readily combine to provide the oscillation time as

$$\tau(r, p_r, p_\theta) = 2m \int_{r_{c0}(r,p_r,p_\theta)}^{r_{c1}(r,p_r,p_\theta)} \frac{dr'}{p_r(r', r, p_r, p_\theta)}, \tag{19}$$

where $r_{c1}(r, p_r, p_\theta)$ and $r_{c0}(r, p_r, p_\theta)$ are the values of r' corresponding to the solution of

$$p_r(r', r, p_r, p_\theta) = 0. \tag{20}$$

It is now necessary to consider the distributions of p_r and p_θ in order to determine the mean value of τ for the particles in the pore space. For the system under investigation these will follow the canonical distribution

$$\psi(r, \theta, z, p_r, p_z, p_\theta) = \psi_0 \exp\left[-\beta\left(\phi_{fs}(r) + \frac{p_r^2}{2m} + \frac{p_\theta^2}{2mr^2}\right)\right], \tag{21}$$

with $\beta = 1/k_B T$, which is the form attained for a constant-temperature system with no correlation between particle states.[22] Averaging of the oscillation time τ in Eq. (19) with respect to the above distribution and substitution into Eq. (9) now provides the low-density transport coefficient

$$D_{t0}^{\mathrm{LD}} = \frac{2}{\pi m Q}\int_0^\infty e^{-\beta\phi_{fs}(r)}dr \int_0^\infty e^{-\beta p_r^2/2m}dp_r \times \int_0^\infty e^{-\beta p_\theta^2/2mr^2}dp_\theta \int_{r_{c0}(r,p_r,p_\theta)}^{r_{c1}(r,p_r,p_\theta)} \frac{dr'}{p_r(r', r, p_r, p_\theta)}, \tag{22}$$

where $Q = \int_0^\infty r e^{-\beta\phi_{fs}(r)}dr$ and $p_r(r', r, p_r, p_\theta)$ follows Eq. (18). This result may be expected to be valid under conditions at which intermolecular interactions are insignificant.

Development of an exact theory such as that above for higher densities, where intermolecular interactions cannot be neglected, is as yet elusive. Despite vigorous attempts,[7,8] progress in this direction has been limited and the theories remain largely intractable. Here we adopt a simplified approach in which Eq. (22) provides the diffusive contribution, while the second term in Eq. (7) provides the viscous contribution at higher densities, leading to

$$D_{t0}(\hat{\rho}) = D_{t0}^{\mathrm{LD}} + \frac{2k_B T}{\hat{\rho} r_p^2}\int_0^{r_0} \frac{dr}{r\,\eta(\overline{\rho}(r))}\left(\int_0^r r'\rho(r')dr'\right)^2, \tag{23}$$

which, as we shall demonstrate, provides remarkably good predictions over a wide range of densities. Upon comparison with Eq. (7) it is readily evident that D_{t0}^{LD} now essentially represents a surface slip term in a viscous flow model.

III. MODEL SYSTEM AND SIMULATION METHODS

The model developed here is in principle applicable to any system of rigid fluid particles in which the fluid–wall interaction can be described in terms of a single one-dimensional potential field $V(r)$. For the purpose of testing

and validating the above theory, however, we have conducted simulations modeling the flow of methane, treated as an LJ fluid, in cylindrical silica pores having infinitely thick amorphous walls comprised of close-packed LJ sites. The simulations parallel those discussed in detail elsewhere,[12] and we therefore provide here only a brief description. The LJ 12-6 potential is used to model the fluid–fluid and fluid–solid interactions. For methane we use the parameter values $\varepsilon_f/k_B=148.1\,\mathrm{K}$, $\sigma_f=0.381\,\mathrm{nm}$, while for the solid we use $\varepsilon_s/k_B=290\,\mathrm{K}$, $\sigma_s=0.29\,\mathrm{nm}$.[12] The one-dimensional fluid–solid potential at any position is obtained by summing over the interaction of an LJ methane particle at that position with sites lying up to 5 atomic diameters on either side. The Lorentz–Berthelot rules are applied to estimate fluid–solid LJ parameters, and a total of 12 layers of sites in the pore wall are used in the summation. A cutoff distance of 1.5 nm is used in estimating fluid–fluid interactions.

In the molecular dynamics computations conducted particle trajectories are obtained by solving the equations of motion

$$\ddot{\mathbf{r}}_i=-\frac{1}{m}\sum_{j\neq i}\nabla_i\Phi_{ij}+\Gamma-\lambda(t)\dot{\mathbf{r}}_i \tag{24}$$

using a fifth-order Gear technique with a time step of 1 fs. Here $\lambda(t)$ is a thermostat factor determined by the Gaussian thermostatting technique[23] employed for temperature control, Φ_{ij} is the potential energy of the i-j interaction, and Γ is a constant acceleration applied to every particle in NEMD simulations. For EMD simulations $\Gamma=0$. The run length is typically $8\times10^6-10\times10^6$ time steps, the first 4×10^4 steps of which are rejected. A diffuse scattering condition is applied at the wall so that, on reversing direction (i.e., reflection) when closer to the wall than the potential minimum, the tangential and axial components of the particle velocity are randomized while conserving kinetic energy. The simulations are started with an initial configuration having about 500 particles, generated using grand canonical Monte Carlo (GCMC) simulations following the Metropolis algorithm.[24] Model isotherms were also determined using the same algorithm.

In the present work transport coefficients of methane have been determined using both EMD and NEMD in cylindrical silica pores of various diameters in the range of 0.75–5.4 nm at temperature of 450 K and for various temperatures in the range of 300–500 K for a pore diameter of 3.01 nm. In the EMD simulations a collective transport coefficient is obtained from the autocorrelation of the fluctuating axial streaming velocity of the system via the Green–Kubo relation[10]

$$D_{t0}=N\lim_{\tau\to\infty}\int_0^\tau\langle u_z(0)u_z(t)\rangle dt, \tag{25}$$

where

$$u_z(t)=\frac{1}{N}\sum_{i=1}^{N}\frac{dz_i}{dt}=\frac{1}{N}\sum_{i=1}^{N}v_{iz}(t) \tag{26}$$

is the instantaneous streaming velocity. In EMD where no external driving force is applied the time-averaged system streaming velocity must vanish; however, the momentum loss due to diffuse reflection at the wall leads to a fluctuating instantaneous streaming velocity whose autocorrelation is exploited to yield the collective transport coefficient pertinent to practical applications.[10–12] In the NEMD computations a constant axial acceleration $\Gamma_z\,(=f/m)$ in the range of 0.001–0.02 nm/ps^2 is applied to particles and an effective transport coefficient D_{t0} computed from the measured flux following

$$j_z=\frac{D_{t0}\hat{\rho}m}{k_BT}\Gamma_z, \tag{27}$$

where j_z is the axial number flux and $\hat{\rho}$ is the average number density of methane in the pore:

$$\hat{\rho}=\frac{2}{r_p^2}\int_0^{r_p}r\rho(r)dr=\frac{N}{V}. \tag{28}$$

Here r_p is the radius corresponding to the first layer of solid atoms and V the volume of the pore used in the simulation. Linear response behavior with transport coefficient independent of the applied acceleration is obtained for the range of Γ_z used.

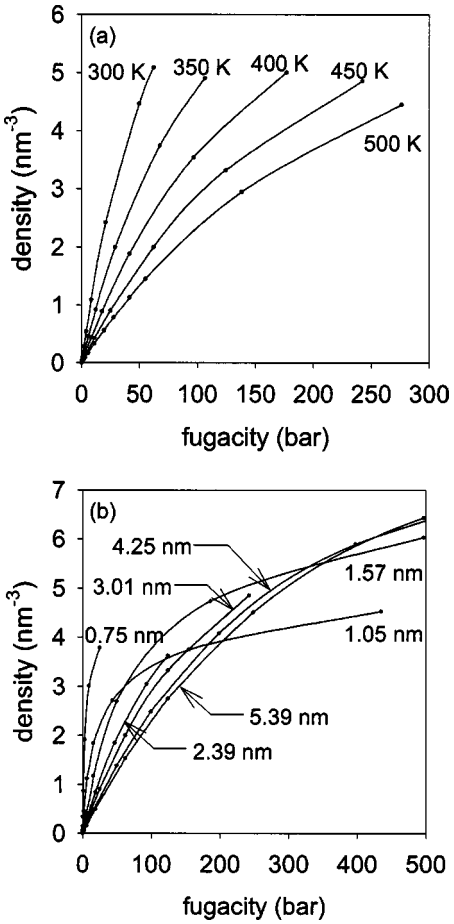

FIG. 2. Methane adsorption isotherms (a) at various temperatures in a silica nanopore of diameter 2.39 nm, and (b) in nanopores of various diameter at 450 K.

IV. RESULTS AND DISCUSSION

A. Classical hard sphere theory

Equation (22) provides the low-pressure transport coefficient in the presence of a one-dimensional potential field in a cylindrical pore, which is more general than the classical Knudsen theory developed for noninteracting systems. The zero-interaction limit may be derived from the present result by substituting $\phi_{fs}=0$, $r\leqslant r_{ph}$ and $\phi_{fs}\to\infty$, $r>r_{ph}$. Here r_{ph} is the radius of the available pore space given by $r_{ph}=r_p-\sigma_{fs}^h$, where σ_{fs}^h is the sum of the radius of the methane and silica surface hard sphere particles. In this case the inner boundary of the oscillation, r_{c0}, is obtained from solution of Eqs. (18) and (20) as

$$r_{c0}=\frac{rp_\theta}{\sqrt{r^2p_r^2+p_\theta^2}}, \tag{29}$$

while $r_{c1}=r_{ph}$. Equations (18) and (22) now yield

$$D_{t0}^{\mathrm{LD}}=\frac{2}{\pi mQ}\int_0^{r_{ph}}dr\int_0^\infty e^{-\beta p_r^2/2m}dp_r\int_0^\infty e^{-\beta p_\theta^2/2mr^2}dp_\theta \times\int_{r_{c0}(r,p_r,p_\theta)}^{r_{ph}}\frac{dr'}{\sqrt{p_r^2+p_\theta^2(r^{-2}-r'^{-2})}}, \tag{30}$$

with $Q=r_{ph}^2/2$. It is straightforward to perform the above integrations and obtain the result

$$D_{t0}^{\mathrm{LD}}=\frac{4r_{ph}}{3}\sqrt{\frac{2k_BT}{\pi m}}, \tag{31}$$

which holds in the presence of only hard sphere interactions. This is precisely the well-known Knudsen result[1,5,6] and illustrates the versatility of the present approach that can consider arbitrary fluid–solid interaction potentials of the form $\phi_{fs}(r)$. In what follows we discuss the results for the LJ 12-6 interactions used here for the chosen system of methane in cylindrical silica pores, using both simulation and theory.

B. Supercritical isotherms

Prior to computing transport coefficients, initially supercritical isotherms of methane in the temperature range of 300–450 K were determined by GCMC simulations for a silica cylindrical nanopore of 3.01 nm diameter (measured from centers of the surface sites). Figure 2(a) depicts the isotherms at five different temperatures, showing a linear (i.e., Henry's law) region up to a methane pore density of approximately 1 nm^{-3}. Saturation is not achieved at the supercritical temperatures chosen, despite high fugacities well beyond the range of interest in most chemical processes. Figure 2(b) depicts the effect of pore diameter on the isotherms at 450 K, again showing a Henry's law region up to a density of about 1 nm^{-3} with saturation not being achieved even at high fugacity exceeding 100 bars. Nevertheless, a pore-size-dependent capacity is evident from Fig. 2(b), with the largest pore size having the highest capacity, which may be attributed to the effect of methane–methane intermolecular interactions. At the smallest pore size of 0.75 nm only a single central file of methane particles centered at the pore axis is anticipated, so that viscous effects may be expected to be small at this size. Figures 3(a)–3(d) depict density profiles at various pore sizes, showing only centrally located particles at the smallest diameter of 0.75 nm and essentially monolayer coverage of the whole surface at the larger sizes. At a pore diameter of 1.05 nm the peak is no longer located at the pore axis, but about 0.18 nm away, a distance somewhat smaller than the particle radius. Consequently, successive particles along the axis are staggered in the radial direction, with their interaction inhibiting complete monolayer coverage. Figures 4(a)–4(c) depict different views of particle configurations at this pore size, illustrating the difficulty in accommodating two particles on the same diameter. This is responsible for the apparently lower saturation capacity at this pore size evident in Fig. 2(b). It is also seen that the density profiles from GCMC and EMD, as well as NEMD calculations to be discussed, are essentially identical, indicating that cross-sectional equilibrium is attained during the transport. This feature was also noted in our recent studies for subcritical temperatures[11,12] and justifies the assumption of a uniform chemical potential over the pore cross section in the integration of Eq. (4).

C. Low-density transport

Transport coefficients at 450 K were subsequently determined using EMD and NEMD, as described earlier, for various pore sizes at low densities ($\rho<0.8$ nm^{-3}) in the Henry's law region. At these conditions the transport coefficient was essentially independent of density, and both EMD and NEMD yielded similar results, as will be subsequently discussed. The latter is in agreement with recent reports[11,12] from this laboratory for transport at subcritical temperatures. Figure 5 depicts the computed variation of the transport coefficient of methane with pore diameter at 450 K, as well as the theoretically predicted results based on Eq. (22). The MD results represent an average value taken over 6–10 runs of 10^7 time steps at adsorbed densities below 0.5 nm^{-3} and are given by the symbols with the error bars depicting the standard deviation. The standard deviation lies in the range of 5%–10% of the mean, although the error bars appear insignificant on the scale of the figure. Excellent agreement between simulation and theory is seen, consistent with our assertion that Eq. (22) provides an exact result for the transport coefficient under conditions of diffuse reflection. Both EMD and NEMD are seen to provide consistent results, in agreement with the earlier results at subcritical conditions. The excellent agreement is evident even at the small pore diameter of 0.75 nm for which only single-file diffusion can occur since the peak in the density profile lies at the pore axis [cf. Fig. 3(a)]. Also shown as the dash-dotted line in Fig. 5 is the Knudsen result in Eq. (31) with r_{ph} taken as the pore diameter r_p. This line clearly overpredicts the transport coefficient several fold and even by more than an order of magnitude in the single-file region. If, on the other hand, we choose r_{ph} as the radius corresponding to the center of the colliding particles and use $r_{ph}=r_p-\sigma_{fs}^h$, with $\sigma_{fs}^h=0.92\,\sigma_{fs}$ [where $\sigma_{fs}=(\sigma_f+\sigma_s)/2$], the dashed curve is ob-

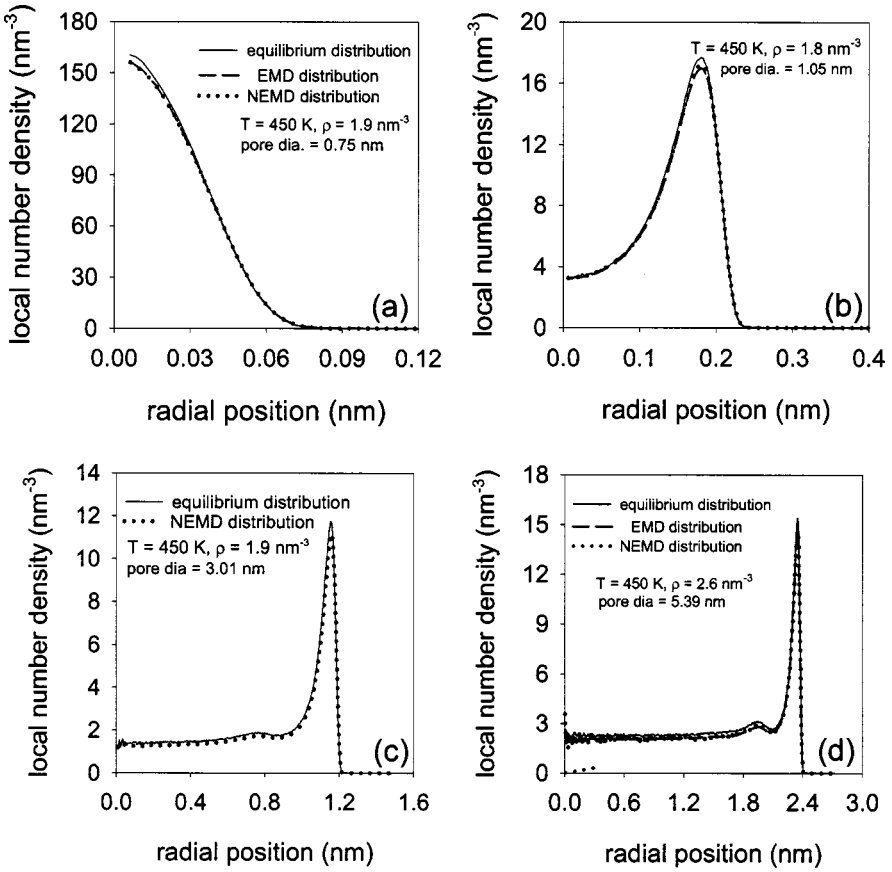

FIG. 3. Radial density profiles at 450 K for various pore sizes and densities, as given in each of parts (a), (b), (c), and (d). Solid lines represent GCMC-determined equilibrium profiles, while dashed lines represent profiles from EMD and dotted lines those from NEMD. In (c) only GCMC- and NEMD-determined profiles are depicted.

tained on the logarithmic coordinates used, which considerably reduces the discrepancy at very small pore sizes. Nevertheless, in mesopores in the range of 2–5 nm considerable error still remains because of the neglect of dispersive interactions in Eq. (31). Such interactions will decrease the oscillation period of the trajectories and consequently reduce the transport coefficient. Physically, the latter occurs because the reduction in period results in lower momentum gain between successive diffuse reflections at the wall.

Besides the comparison of predicted transport coefficients with simulation results, a good test of the theory is the comparison of axial streaming velocity profiles. To this end Eqs. (11)–(13) yield

$$\frac{dp_z}{dr} = \frac{mf}{p_r}, \tag{32}$$

which readily integrates to provide

$$p_z^-(r) = p_{z0} - mf \int_r^{r_{c1}} \frac{dr'}{p_r(r',r,p_r,p_\theta)} \tag{33}$$

for particles moving away from the wall, for which the radial momentum is negative, and

$$p_z^+(r) = p_{z0} + \int_{r_{c1}}^{r_{c0}} \frac{dr'}{p_r(r',r,p_r,p_\theta)} + \int_{r_{c0}}^{r} \frac{dr'}{p_r(r',r,p_r,p_\theta)} \tag{34}$$

for particles moving towards the wall, for which the radial momentum is positive. Equations (33) and (34) combine to provide the mean axial streaming velocity at any radial position as

$$\begin{aligned}\langle v_z \rangle &= \frac{1}{m}[\langle p_z^- \rangle + \langle p_z^+ \rangle] \\ &= \frac{2f}{\pi m r k_B T} \int_0^\infty e^{-\beta p_r^2/2m} dp_r \int_0^\infty e^{-\beta p_\theta^2/2mr^2} dp_\theta \\ &\quad \times \int_{r_{c0}(r,p_r,p_\theta)}^{r_{c1}(r,p_r,p_\theta)} \frac{dr'}{p_r(r',r,p_r,p_\theta)}.\end{aligned} \tag{35}$$

Comparison of velocity profiles predicted by Eq. (35) with simulation results gave excellent agreement in all cases. As an example, Fig. 6 depicts the agreement for a pore of diameter 2.39 nm at 450 K and density of 0.18 nm^{-3}, with an applied acceleration of 0.015 nm/ps^2.

NEMD calculations were also performed of the transport coefficient in a pore of diameter 3.01 nm at various temperatures in the range of 300–500 K, and the results are depicted by the symbols in Fig. 7. As in Fig. 5, the MD values represent an average of 6–10 runs of 10^7 time steps, and the superimposed error bars represent the corresponding standard deviation. The theoretical values are also shown in the figure, represented by the solid line, again demonstrating excellent agreement between theory and simulation. Good linearity on the Arrhenius coordinates used is also evident, with the linear regression line (dashed) yielding an apparent acti-

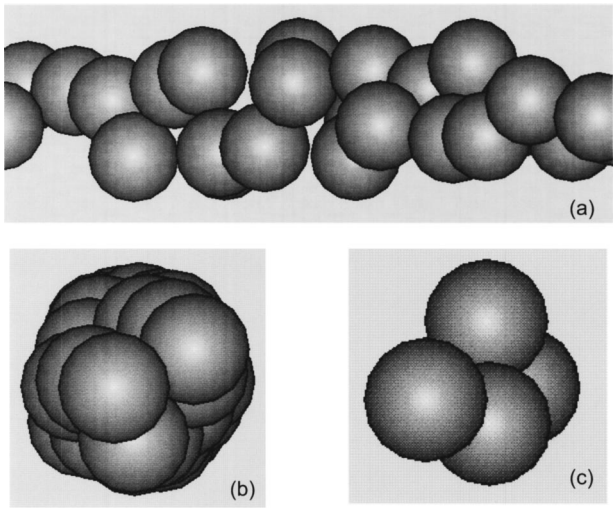

FIG. 4. Sample configurations of LJ methane particles in a 1.05-nm-diam pore. (a) Side view and (b) cross-sectional view, at density of 4.5 nm^{-3}. (c) Cross-sectional view at density of 0.45 nm^{-3}.

vation energy of 5.69 kJ/mol. This is construed as an ''apparent'' value because in principle there is no activation barrier to the axial transport in pores with a uniform surface as assumed here. However, because the oscillating molecules possess different energies depending on the values of r_{c0} and r_{c1}, an apparent activation energy may be associated with the energy suitably averaged over the trajectories, in excess of the underlying mean potential energy. More precisely, we may define an activation energy as

$$E = -\frac{d \ln D_{t0}^{\mathrm{LD}}}{d\beta}, \tag{36}$$

which combines with Eqs. (13), (14), (16), and (22) to provide

$$E = \frac{\langle (H - p_{z0}^2/2m)\tau \rangle}{\langle \tau \rangle} - \langle \phi \rangle. \tag{37}$$

Physically, this may be construed as the excess of a suitably averaged Hamiltonian over the sum of the average potential energy and axial kinetic energy, and therefore in a loose sense an average of the total radial and angular kinetic energies. For comparison with the activation energy of 5.69 kJ/mol in Fig. 7, at the temperature of 400 K (midpoint of the temperature range used) we estimate the mean total radial and angular kinetic energy as 3.326 kJ/mol ($N_0 k_B T$, where N_0 is the Avogadro number), which is slightly lower. However, from Eq. (37) it is evident that the apparent activation energy is biased towards the longer trajectories having higher kinetic energies, justifying its significantly higher value.

To determine the effect of pore size on the activation energy, theoretical values of the low-density transport coefficient at various temperatures in the range of 300–500 K have been determined and are depicted in Fig. 8. The Arrhenius character of the temperature dependence over this narrow temperature range is clearly evident, for the several pore sizes used, with the apparent activation energy reducing with decrease in pore diameter. Figure 9 depicts the variation in apparent activation energy with pore diameter, determined from the slopes of the lines in Fig. 8. The increase in apparent activation energy with increase in pore diameter is most

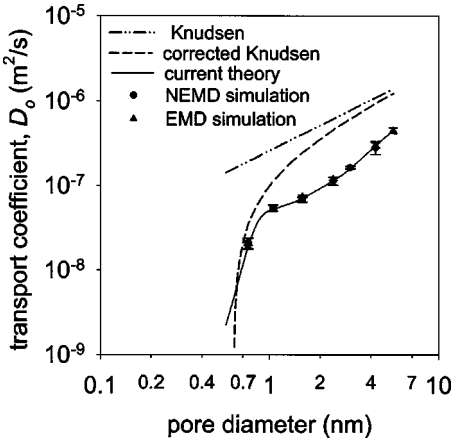

FIG. 5. Comparison of simulation and predicted variation of low-density transport coefficient with pore diameter for methane at 450 K.

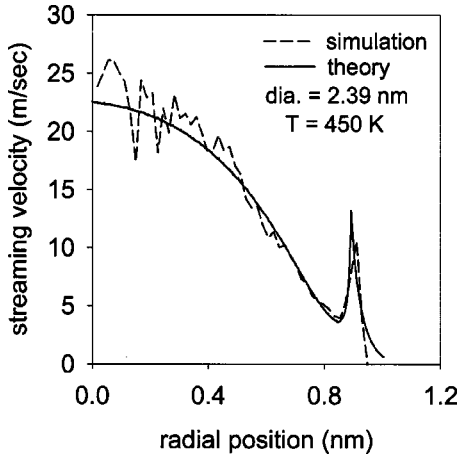

FIG. 6. Comparison of simulation and predicted velocity profiles in a 2.39-nm-diam pore at density of 0.18 nm^{-3} at 450 K, for an applied acceleration of 0.015 ps/nm^2.

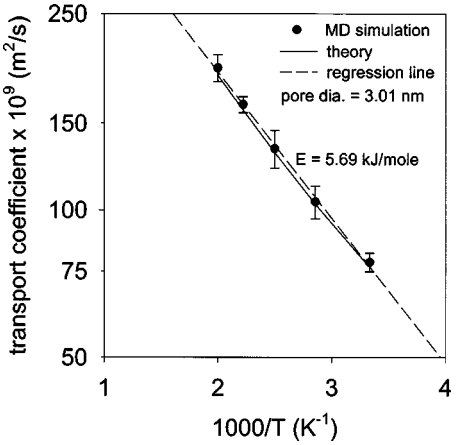

FIG. 7. Predicted and simulation results for variation of low-density transport coefficient with temperature for a 3.01-nm-diam pore. The dashed line represents linear regression of the MD data on the semi logarithmic coordinates used.

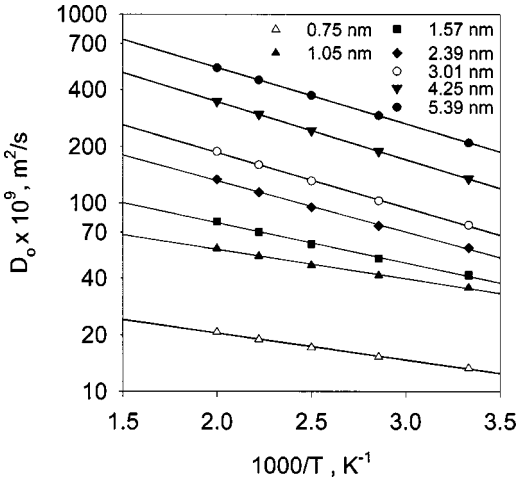

FIG. 8. Theoretically predicted variation of the low-density transport coefficient with temperature for various pore diameters. Symbols represent theoretical results and solid lines linear regression on the semilogarithmic coordinates used.

prominent at small pore sizes in the micropore range (<2 nm diameter), above which it is almost constant. Also superimposed in the figure is the variation in the magnitude of the minimum potential energy with pore diameter, showing an opposite trend to the activation energy. This is a rather interesting result as it is in contradiction to the conventional empirical assumption that the activation energy for diffusion is proportional to the heat of adsorption[4] or the magnitude of the minimum potential energy—i.e., $E=a|\phi_{\min}|$ where $0.3<a<1$. The discrepancy is, however, readily resolved by Eq. (37), which suggests that the activation energy is instead related to the excess of the suitably averaged Hamiltonian (excess over the mean potential energy) representing a temperature-dependent potential barrier.

D. Variation of transport coefficient with density

Following the success of the low-density theory, as discussed above, computations of the density variation of the transport coefficient at 450 K were done for various pore sizes in order to test the adequacy of the expression in Eq. (23) and to compare it with its predecessor in Eq. (7). Figures 10(a), 10(b), and 10(c) depict the results for pore diameters of 0.75 nm, 1.05 nm, and 1.57 nm, respectively, lying in the micropore region, with solid circles representing transport coefficients determined by NEMD and solid triangles those determined by EMD. Although the standard deviation was not determined at every density, it was found that at the low density the transport coefficient varied by less than 10% in repeat runs with different initial configurations at selected densities, while at high density this variation was within 5%. While this was predominantly the case, for the NEMD at low densities a few points (less than 5% of the NEMD runs) showed significantly larger statistical deviation and were ignored. Consistent with our earlier work for mesopores,[11,12] there is good agreement between the EMD and NEMD values of the coefficient, confirming their equivalence in the micropore region as well. This is also consistent with other literature reports[25,26] for diffusion in micropores and is to be expected given their agreement for mesopores where viscous flow is very significant and can even dominate over the purely diffusive part. In micropores the latter is expected to provide the major contribution to the flow, with viscous transport being considerably weaker. This behavior is indeed evident in Fig. 10, where the transport coefficient is essentially independent of density for the 0.75-nm-diam pore. For the larger micropores in Figs. 10(b) and 10(c) some increase in transport coefficient is evident at densities above about 0.5 nm^{-3}, suggesting the onset of viscous flow. At the pore diameter of 1.05 nm there is a subsequent rapid decline in the transport coefficient beyond a density of about 1.5 nm^{-3}, to levels well below the Henry's law region. This is attributed to the lack of complete monolayer coverage, with successive methane molecules being staggered in the axial direction, as depicted in Fig. 4. With an increase in density intermolecular interactions between neighboring molecules on opposite sides considerably increase the frequency of wall reflections and therefore reduce the period of oscillation of the molecules. This leads to a sharp decline in the transport coefficient. In this situation the molecules oscillate in a narrow region near the wall, and the transport can be likened to creeping of the molecules along the potential minimum surface. This creeping behavior is somewhat reminiscent of the floating molecule concept first discussed by Derouane *et al.*[27] and subsequently elaborated by Yashonath and co-workers[28,29] with regard to diffusion in zeolites. However, it is to be noted that in these cases the creeping behavior is due to the relative strength of the fluid–solid interaction potential compared to the kinetic energy, as opposed to effect of the fluid–fluid interaction in the present case.

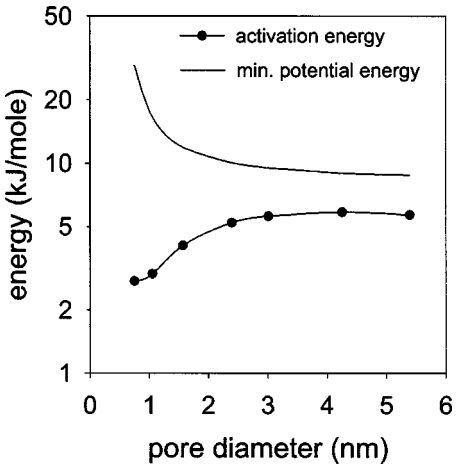

FIG. 9. Variation of activation energy and minimum potential energy in pore with pore diameter.

Figures 10(a)–10(c) also depict the results based on Eqs. (7) and (23), shown as the dashed and solid lines, respectively. For the calculations the density profile obtained from GCMC simulations was used, and the viscosity determined using the correlation of Chung *et al.*[30] at the locally averaged density following Eq. (3). As seen in the figures, the calculations (solid lines) based on Eq. (23) can represent the density variation of the transport coefficient very well up to the maximum, but the subsequent decline is somewhat less

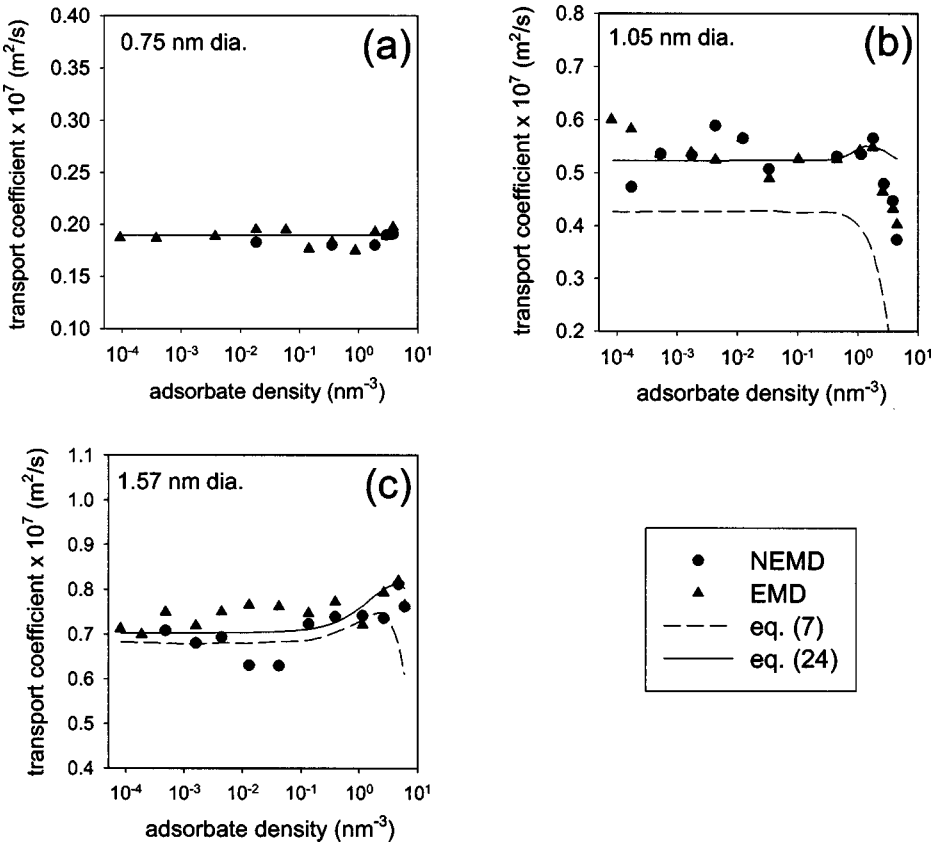

FIG. 10. Variation of transport coefficient with adsorbed methane density at 450 K, based on MD simulation and theory, for micropores of diameter (a) 0.75 nm, (b) 1.05 nm, and (c) 1.57 nm.

steep. This is largely because use of the Henry's law transport coefficient in the first term on the right-hand side overlooks the decline in oscillation period due to intermolecular interactions at high density. Further refinement of the approach to consider such interactions is therefore suggested and will be examined in the future. Nevertheless, it is evident that the new approach is a considerable improvement over the earlier one in Eq. (7), given by the dashed curves in Figs. 10(a)–10(c), which underpredicts the Henry's law transport coefficient. The latter is most likely due to the assumption of a colliding system of particles at the potential minimum, and thereby an uncorrelated Maxwellian distribution of velocities, in invoking the kinetic theory based collision frequency at this position. At very low densities such intermolecular collisions are infrequent, and only the wall–fluid interaction need be considered. A further feature of the dashed curves in Fig. 10 is that at the smallest diameter of 0.75 nm, where the potential minimum is at the pore center, $r_0=0$, and Eq. (7) incorrectly yields a vanishing transport coefficient. On the other hand, Eq. (23) accurately predicts the behavior with a vanishing viscous part due to the absence of particle crossing.

Figures 11(a)–11(d) depict the simulation and theoretical results for various pore diameters in the mesopore range. The symbols and dashed as well as solid lines have the same significance as in Fig. 10. As expected,[11,12] both EMD and NEMD coefficients match. In performing the computations it was found that NEMD results had greater scatter at low densities, most likely because of the relatively larger ''noise'' in this region where small accelerations must be used to ensure linear response behavior. At high densities, however, it is the EMD coefficient that is more affected by the ''noise.'' As seen in Fig. 11, the solid line representing the results from Eq. (23) can predict the density dependence of the transport coefficient remarkably well, though at high densities beyond about 5 nm^{-3} it overpredicts slightly most likely because of the neglect of the effect of intermolecular interactions on the oscillation period in the first term on the right-hand side. Since the coefficient D_{t0}^{LD} represents a slip contribution, it is evident that the model does not accurately capture the processes, leading to a reduction in surface slip at very high density, which was also evident in our earlier studies.[11,12] Nevertheless, this effect occurs at very large bulk fugacities, as seen from the isotherms in Fig. 2, and for most practically significant systems Eq. (23) performs remarkably well. On the other hand, the model of Eq. (7) somewhat underpredicts due to underestimation of the low-density transport coefficient. At high densities, however, the predictions of Eqs. (7) and (23) approach each other, because of dominance of the viscous term in these models. In Eq. (23) the first term on the right-hand side is independent of density, so the entire density dependence arises from the viscous term, and the agreement with simulations in the density-dependent region, beyond a density of about 0.5 nm^{-3}, confirms this to be adequate. In particular, it is clear that the steep increase in transport coefficient in this region is due to the rapid onset of viscous flow.

The effect of temperature on the density variation of the transport coefficient was also investigated at the pore diameter of 3.01 nm. Figures 12(a)–12(d) depict the results of simulation and theory, with symbols and lines having the

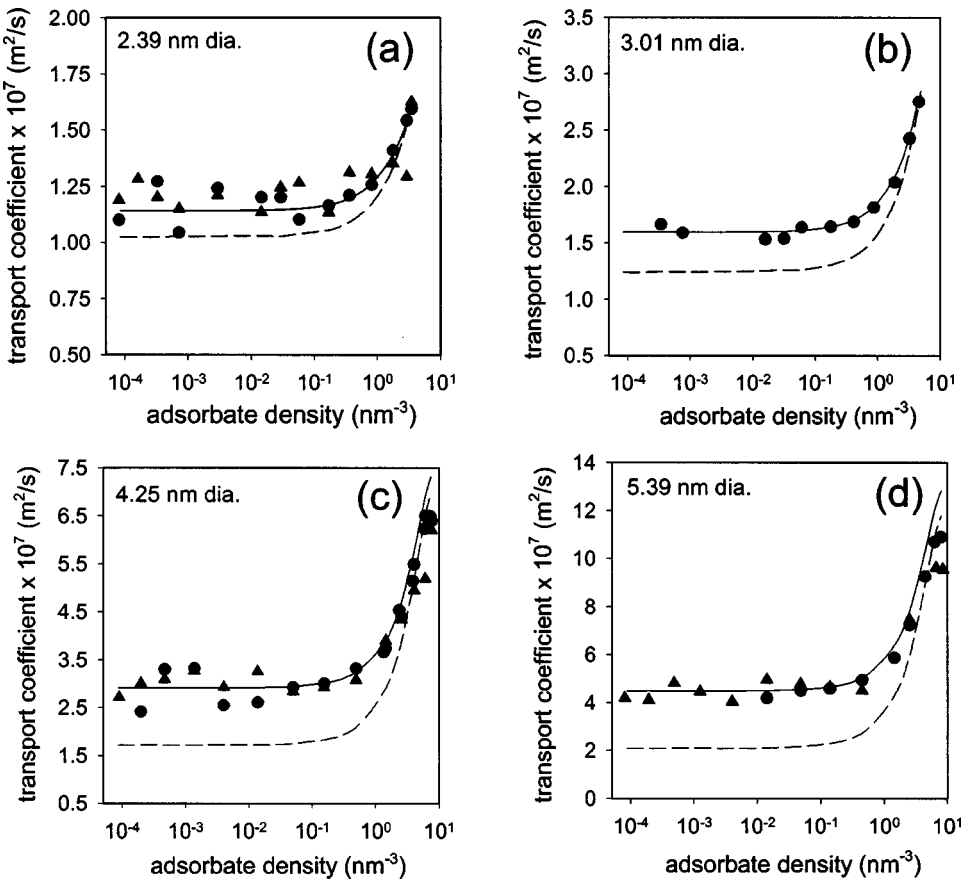

FIG. 11. Variation of transport coefficient with adsorbed methane density at 450 K, based on MD simulation and theory, for mesopores of diameter (a) 2.39 nm, (b) 3.01 nm, (c) 4.25 nm, and (d) 5.39 nm.

same significance as in Fig. 10. As in Figs. 10 and 11, it is evident that the solid line, representing calculations based on Eq. (23), predicts the simulation results remarkably well at all temperatures, while Eq. (7) using the kinetic theory based friction factor slightly underpredicts. The steep increase in transport coefficient beyond a density of about 0.5 nm^{-3} is clearly due to viscous effects arising out of intermolecular interactions, evident from the good agreement of the theory in Eq. (7), as discussed earlier.

Figure 13(a) depicts the theoretical relative contribution of viscous flow to the transport coefficient at 450 K, based on Eq. (23), for the various pore sizes in Figs. 10 and 11. With an increase in pore diameter the viscous contribution at any density is higher, as expected. In the mesopore range ($>$2 nm diameter) the transport coefficient increases monotonically with density, while in micropores ($<$2 nm diameter) there is a decrease in viscous contribution at a sufficiently high density as discussed earlier. This decrease is particularly severe for the 1.05-nm-diam pore where complete monolayer coverage cannot be achieved (cf. Fig. 2) and intermolecular interactions lead to a reduced oscillation period. At the smallest pores size of 0.75 nm there is only a central file of molecules and viscous flow is essentially absent. Figure 13(b) depicts the effect of temperature on the fraction of viscous flow for the pore diameter of 3.01 nm, indicating only weak dependency at a given density. There is a modest increase in fraction of viscous flow with temperature, suggesting a strong decrease in viscosity with increase in temperature in comparison to the effect on the low-density transport coefficient.

It is clear that the new theory offers an attractive option for the accurate prediction of low-density transport coefficients in nanopores from first principles and also the density dependence of the transport coefficient using the LADM, overcoming the empiricism in existing approaches.[4] At low densities, where fluid–fluid interactions are insignificant, the self- and transport diffusivities are identical and are exactly determined from the present theory. As seen above, this transport diffusivity is constant over a range of densities of practical importance (less than about 1 nm^{-3}) under supercritical conditions. This holds even for single-file diffusion, as shown in Fig. 10(a) for methane transport at 450 K in a 0.75-nm-diam silica pore, in which only one layer can be accommodated. In this case it was noted that this transport diffusivity, obtained using NEMD as well as EMD, is constant at the low density value predicted remarkably well by the theory. The density variation of the transport coefficient is predominantly due to viscous effects, which are absent in single-file diffusion where particle crossings are rare. For the single-component case it is easily seen that intermolecular ''collisions'' cannot affect the collective transport coefficient in *true* single-file diffusion, where the interaction force is purely in the axial direction. As a result, the lateral oscillation period is not affected and, because intermolecular interactions exert no *net* force on the system, the center-of-mass motion is also unaffected. Consequently, the transport diffusivity will be independent of density, which is confirmed by Fig. 10(a). On the other hand, it is known[31–33] that self-diffusion is nonclassical with mean-squared displacement

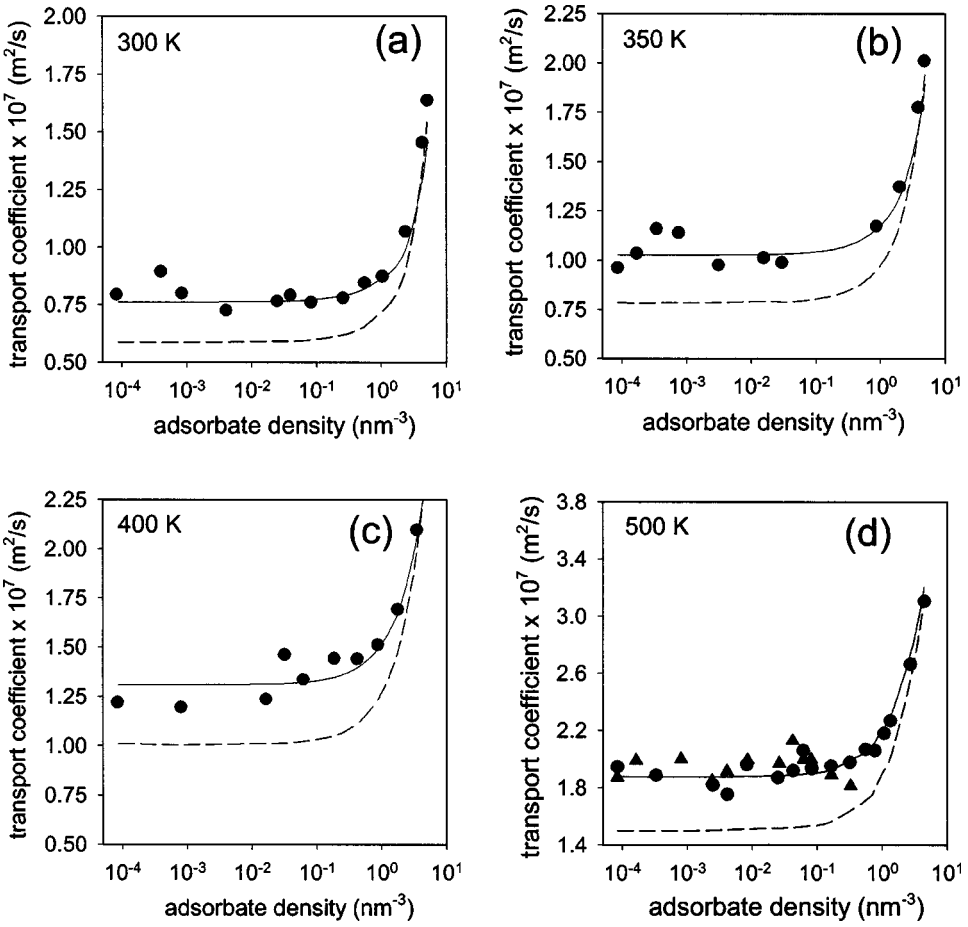

FIG. 12. Variation of transport coefficient with adsorbed methane density for mesopore of diameter 3.01 nm, based on MD simulation and theory, at temperature of (a) 300 K, (b) 350 K, (c) 400 K, and (d) 500 K.

$\langle z^2 \rangle \propto \sqrt{t}$ when intermolecular "collisions" dominate. The classical nature of the transport diffusivity (i.e., following the Einstein relation) is evident in Fig. 14(a), illustrating linearity of the mean-squared displacement of the center of mass, $\langle z^2 \rangle_{cm}$, with time, at long time, obtained using EMD, at low ($8 \times 10^{-5}\,\mathrm{nm}^{-3}$) and high ($3.84\,\mathrm{nm}^{-3}$) density. However, for $\langle z^2 \rangle$ the long-time slope is unity at the low density and approaches 0.7 at high density, as seen in Fig. 14(b), indicating a transition to nonclassical behavior for the self-diffusion when intermolecular interactions become important. Thus the value of the present theory in predicting the correct transport diffusivity pertaining to the collective motion, which is consistent with the classical Einstein relation, is clearly evident.

The above results are consistent with recent findings with regard to transport in silicalite and shed much light on the well-known problem of diffusion in narrow-pore zeolites where single-file motion predominates. Concentration-independent diffusivities of methane in silicalite have indeed been observed experimentally as well as by MD simulation[34,35] and are now readily explained as above. It should be noted that in these studies the applicability of the Darken equation has been verified for the Fickian transport diffusivity based on a concentration gradient driving force, showing that the corrected diffusivity based on a chemical potential driving force (which is equivalent to our transport coefficient D_{t0}) is concentration independent. On the other hand, there are also contrary observations, such as those of CF_4 transport in silicalite,[34] in which the corrected diffusivity is not concentration independent. However, such results are most likely a reflection of significant intermolecular interactions among molecules in neighboring pores of the three-dimensional silicalite pore network. While not significant for methane such interactions may be important for heavier molecules such as CF_4, but are not considered in our analysis, which is currently based on a single one-dimensional cylindrical pore. Indeed, the existence of such interpore interactions is also suggested in earlier work showing differences in calculated neutron diffraction spectra for methane adsorbed in $AlPO_5$, between calculations based on one and 16 pores in a unit cell.[36] Similarly, there are also observations of differences between self- and transport diffusivities at low densities due to geometric heterogeneities in rough pores,[37] which are not predicted here because the momenta of different molecules are uncorrelated in the absence of fluid–solid interactions for the smooth pores considered. Nevertheless, our theory is quite flexible and can be extended to consider more complex pore topologies as well as potentials, albeit with greater computational burden. Boundary conditions other than that of diffuse reflection employed here can also be investigated. In the future we hope to address such problems.

V. CONCLUSIONS

The results of this work demonstrate that at low densities the molecular trajectories in nanopores can be conveniently

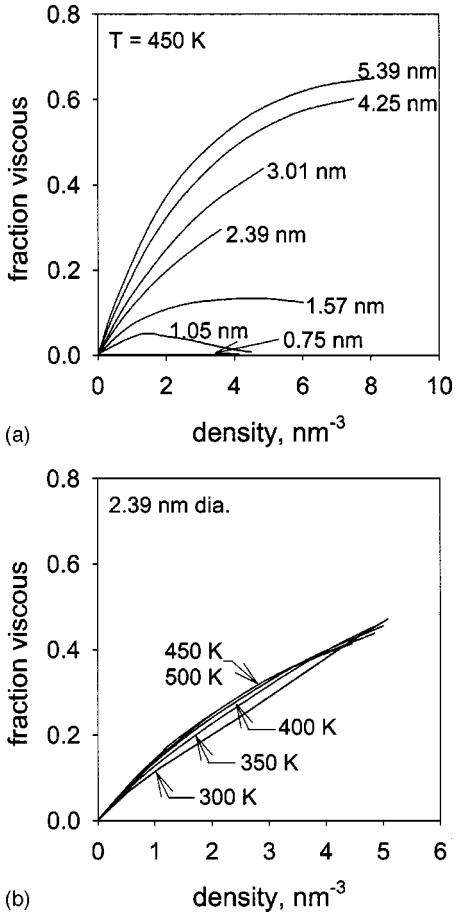

FIG. 13. Variation of relative contribution of viscous flow to transport coefficient as a function of adsorbed methane density (a) for various pore diameters at 450 K and (b) at various temperatures for a mesopore of diameter 3.01 nm.

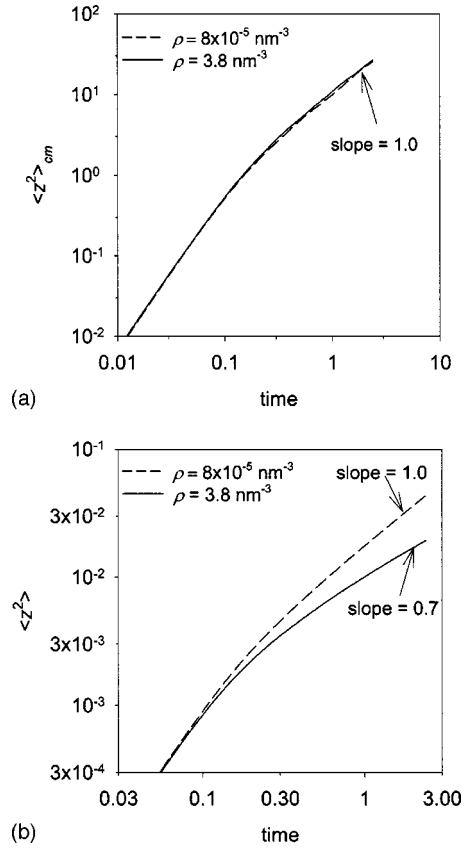

FIG. 14. Temporal variation of the mean-squared displacement (a) of the center of mass and (b) of a single particle at 450 K for low as well as a high density for single-file transport in a micropore of diameter 0.75 nm.

analyzed as oscillatory motion between diffuse wall reflections to yield an axial transport coefficient based on the average momentum gained in a single oscillation. Although we have considered only diffusely reflecting walls, other boundary conditions, such as partially specular reflections or those arising from atomically detailed surfaces,[15–17] can also be utilized instead, albeit at increased computational burden. Nevertheless, the success of the theory now obviates the need for MD calculations of transport coefficients for LJ fluids in nanopores at low density, at least with diffusely reflecting walls. Besides the elimination of statistical noise inherent to MD simulations, the theory provides immense computational advantage, reducing CPU time from several days for the 10^7 time steps used in the MD the simulations to only about 20–45 min for the theory. The latter also accurately predicts the collective Fickian-transport-coefficient for single-file transport pertinent to actual applications, as opposed to the more conventionally studied self-diffusion coefficient that is non-Fickian. In addition, the theory can be readily extended for other pore shapes, such as slit pores.[14]

While proving accurate and essentially exact at low density at all pore sizes, the theory contradicts commonly used empirical representations relating activation energy to the minimum potential energy or isosteric heat of adsorption in the pore. Instead, it appears that the activation energy is more closely related to the excess of a suitably averaged Hamiltonian over the average potential energy in the pore and is better represented as a pore-size-dependent function of temperature. Further, with an increase in density the transport coefficient increases as intermolecular interactions become significant. These interactions can be conveniently incorporated in terms of an additional viscous flow term, using the recently developed refinement[11,12] of the LADM, which provides accurate predictions of the transport coefficient over a wide range of densities. In micropores and mesopores, however, the procedure somewhat overpredicts at very high bulk fugacity, due to the large reduction in oscillation period not represented by the present approach. Further studies along these lines are underway and will be reported in due course.

ACKNOWLEDGMENT

This research has been supported by the Australian Research Council under the Large Grants Scheme.

[1] M. Knudsen, Ann. Phys. (Leipzig) **28**, 75 (1909).
[2] M. E. Davis, Nature (London) **417**, 813 (2002).
[3] P. Selvam, S. K. Bhatia, and C. G. Sonwane, Ind. Eng. Chem. Res. **40**, 3237 (2001).
[4] J. Kärger and D. M. Ruthven, *Diffusion in Zeolites and other Microporous Solids* (Wiley, New York, 1992).
[5] von Smoluchowski, Ann. Phys. (Leipzig) **33**, 1559 (1910).
[6] W. G. Pollard and R. D. Present, Phys. Rev. **73**, 762 (1948).
[7] H. T. Davis, in *Fundamentals of Inhomogenous Fluids*, edited by D. Henderson (Dekker, New York, 1992).

[8] L. A. Pozhar and K. E. Gubbins, Int. J. Thermophys. **20**, 805 (1999).
[9] E. A. Mason, A. P. Malinauskas, and R. B. Evans, J. Chem. Phys. **46**, 3199 (1967).
[10] D. Nicholson and K. Travis, in *Recent Advances in Gas Separation by Microporous Membranes*, edited by N. Kanellopoulos (Elsevier, Amsterdam, 2000).
[11] S. K. Bhatia and D. Nicholson, Phys. Rev. Lett. **90**, 016105 (2003).
[12] S. K. Bhatia and D. Nicholson, J. Chem. Phys. **119**, 1719 (2003).
[13] I. Bitsanis, T. K. Vanderlick, M. Tirrell, and H. T. Davis, J. Chem. Phys. **89**, 3152 (1988).
[14] O. Jepps, S. K. Bhatia, and D. J. Searles, Phys. Rev. Lett. **91**, 126102 (2003); J. Chem. Phys. (in press).
[15] V. P. Sokhan, D. Nicholson, and N. Quirke, J. Chem. Phys. **115**, 3878 (2001).
[16] V. P. Sokhan, D. Nicholson, and N. Quirke, J. Chem. Phys. **117**, 8531 (2002).
[17] A. I. Skouladis, D. M. Ackerman, J. K. Johnson, and D. S. Scholl, Phys. Rev. Lett. **89**, 185901 (2002).
[18] B. Feng and S. K. Bhatia, Carbon **40**, 481 (2002).
[19] H. Shi, J. N. Reimers, and J. R. Dahn, J. Appl. Crystallogr. **26**, 827 (1993).
[20] T. J. Bandosz, M. J. Biggs, K. E. Gubbins, Y. Hattori, T. Liyama, K. Kaneko, J. Pikunic, and K. T. Thomson, Chem. Phys. Carbon **28**, 41 (2003).
[21] D. Nicholson and J. H. Petropoulos, Ber. Bunsenges. Phys. Chem. **79**, 796 (1975).
[22] D. A. McQuarrie, *Statistical Mechanics* (University Science Books, Sausalito, 2000).
[23] D. J. Evans and G. P. Morriss, *Statistical Mechanics of Nonequilibrium Liquids* (Academic, London, 1990).
[24] A. W. Rosenbluth, M. N. Rosenbluth, A. N. Teller, and E. Teller, J. Chem. Phys. **21**, 1087 (1953).
[25] G. Arya, H.-C. Chang, and E. Maginn, J. Chem. Phys. **115**, 8112 (2001).
[26] D. Nicholson, Mol. Phys. **100**, 2151 (2002).
[27] E. G. Derouane, J.-M. Andre, and A. A. Lucas, J. Catal. **110**, 59 (1988).
[28] S. Yashonath and P. Santikary, J. Phys. Chem. **98**, 6368 (1994).
[29] S. Bandyopadhyay and S. Yashonath, J. Phys. Chem. **99**, 4286 (1995).
[30] T. H. Chung, M. Ajlan, L. L. Lee, and K. E. Starling, Ind. Eng. Chem. Res. **27**, 671 (1988).
[31] K. Hahn and J. Kärger, J. Phys. Chem. B **102**, 5766 (1998).
[32] D. S. Sholl and K. A. Fichthorn, Phys. Rev. E **55**, 7753 (1997).
[33] K. K. Mon and J. K. Percus, J. Chem. Phys. **117**, 2289 (2002).
[34] T. C. Bowen, J. L. Falconer, R. D. Noble, A. I. Skouladis, and D. S. Scholl, Ind. Eng. Chem. Res. **41**, 1641 (2002).
[35] E. J. Maginn, A. T. Bell, and D. N. Theodorou, J. Phys. Chem. **97**, 4173 (1993).
[36] V. Lachet, A. Boutin, R. J.-M. Pellenq, D. Nicholson, and A. Fuchs, J. Phys. Chem. **100**, 9006 (1996).
[37] K. Malek and M.-O. Coppens, Phys. Rev. Lett. **87**, 125505 (2002).